Nanoscale Advances

ROYAL SOCIETY OF CHEMISTRY

PAPER

View Article Online
View Journal | View Issue

Cite this: *Nanoscale Adv.*, 2023, **5**, 228

Metal nanoparticle-decorated germanane for selective photocatalytic aerobic oxidation of benzyl alcohol†

Chuyi Ni, Madison Chevalier and Jonathan G. C. Veinot *

Received 4th August 2022
Accepted 27th November 2022

DOI: 10.1039/d2na00518b

rsc.li/nanoscale-advances

Two dimensional materials such as germanane have attracted substantial research interest due to their unique chemical, optical, and electronic properties. A variety of methods for introducing diverse functionalities to their surfaces have been reported and these materials have been exploited as photocatalysts. Herein, we report the preparation of metal nanoparticle (Au, Ag, Cu, Pd, Pt) decorated germanane (M@GeNSs) *via* facile surface-mediated reduction and investigate their structure, composition, as well morphology using X-ray diffraction (XRD), Fourier-transform infrared spectroscopy (FTIR), X-ray photoelectron spectroscopy (XPS) and transmission electron microscopy (TEM). These functional materials were subsequently explored as photocatalysts for selective visible light-induced oxidation of benzyl alcohol to benzaldehyde as freestanding nanosystems and thin films and a reaction mechanism of the photocatalytic oxidation of benzyl alcohol is proposed.

Introduction

Germanane and silicane are 2-dimensional semiconductors that comprise atoms bonded in an arrangement approximating that of the atoms on the (100) surfaces of hydrogen-terminated Ge and Si, respectively.[1] These materials possess surface chemistry dependant optical band gaps in the range of 1.4–1.7 eV (germanane)[2] and 2.4–2.6 eV (silicane);[3] several studies have also reported their use as photocatalyst.[4] Visible light irradiation of hydrogen-terminated germanane provided Liu *et al.* with a source of hydrogen from aqueous methanol, as well as a means to photodegrade rhodamine B.[5] These authors later extended this same reactivity to methyl-terminated germanane.[6] Pumera and colleagues expanded upon Liu's studies and explored the reactivity of an array of germananes bearing various surface groups while evaluating the impact of surface chemistry on their photoelectrocatalytic activity in the hydrogen evolution reaction.[7] Taking a different approach, Ozin and co-workers modified silicanes by exploiting the reducing nature of Si–H surfaces and decorated said surfaces with Pd nanoparticles; these materials catalyzed photoreduction of carbon dioxide.[8] Most recently, Zhao *et al.* described yet another approach toward tailoring group 14 element nanosheets with the formation of "siligenes" terminated with a mixture of –H/–OH surface groups. These mixed element 2D materials provided photocatalytic hydrogen evolution from water and carbon dioxide reduction to provide carbon monoxide.[9] All of these studies point to the tunability, intriguing reactivity, and practical potential of 2D nanomaterials based upon group 14 elements.

Drawing inspiration from metal decorated silicane as well as the established reactivity of bulk germanium,[10] we have explored the reactivity of germanane (GeNS) and demonstrated the straightforward deposition of a variety of metal nanoparticles (MNPs) onto their surfaces (Scheme 1).

Selectively oxidizing alcohols to aldehydes so they can be utilized in aldol condensation reactions to form β-hydroxyaldehydes is essential to fine chemical and pharmaceutical syntheses (*e.g.*, the synthesis of cinnamaldehyde).[11] Traditionally, these transformations are achieved using stoichiometric quantities of homogenous chromate- or permanganate-based oxidants that bring with them concerns related to toxicity and responsible disposal.[12] Of late, much effort has been focused on developing alternative reaction schemes including those exploiting sustainable heterogeneous catalysts.[13–15] Many heterogeneous catalysts based upon active noble metals (*e.g.*, Au, Pd, Pt, and their alloys) have been reported.[16,17] Among the new catalytic systems that have been explored for photocatalytic oxidation, metal-decorated semiconductor (*e.g.*, TiO_2, CdS, Bi_2WO_6) substrates that can be light activated have garnered much attention in part because of the advent of efficient light sources that are driving a concerted push to decarbonize industrial chemical conversions.[16,18,19] Herein, we demonstrate that metal-decorated germanane hybrid nanomaterials can catalyze visible light-mediated, solvent-free oxidation of benzyl alcohol (BA) to benzaldehyde (BAL).

Department of Chemistry, University of Alberta, Edmonton, Alberta, Canada T6G 2G2. E-mail: jveinot@ualberta.ca

† Electronic supplementary information (ESI) available. See DOI: https://doi.org/10.1039/d2na00518b

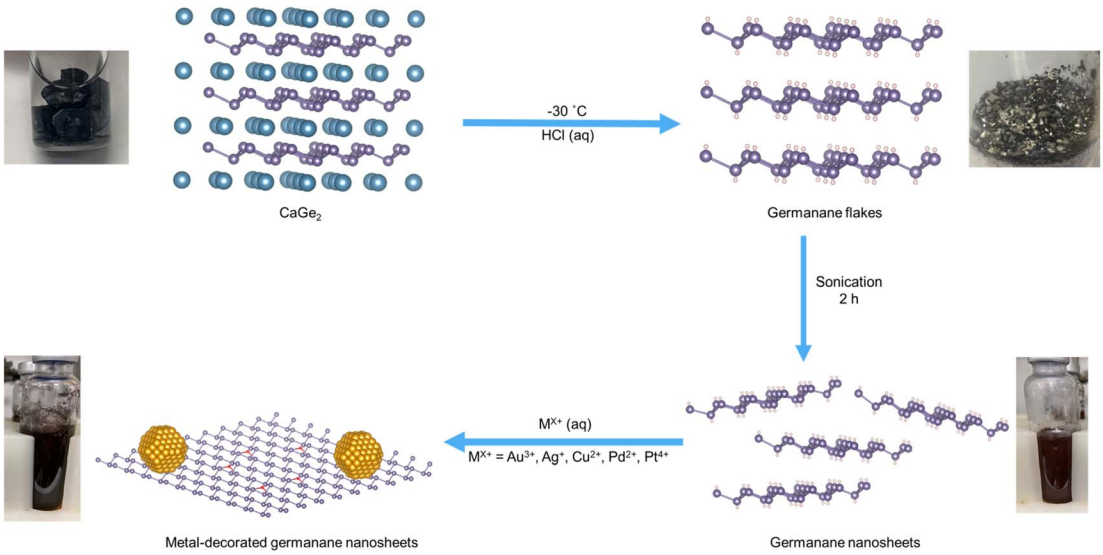

Scheme 1 A pictorial illustration of the formation of metal nanoparticle-decorated germanane. Germanane flakes were prepared *via* topotactic deintercalation of calcium ions from $CaGe_2$. The flakes were subsequently sonicated in Milli-Q water for 2 h to obtain the germanane nanosheets. Aqueous solutions of metal salts (*i.e.*, $AuCl_3$, $AgNO_3$, $CuCl_2$, $PdCl_2$ and $PtCl_4$) were added into the aqueous suspension of germanane nanosheets. Metal ions are reduced to metal nanoparticles and deposited onto the germanane surfaces with the evolution of the bubbles.

Materials preparation and characterization

Germanane used in the present study was prepared *via* topotactic deintercalation of calcium digermanide (Scheme 1).[20] The product of the deintercalation was sonicated for 2 h in water to maximize exfoliation of GeNSs that were immediately combined with aqueous solutions containing the metal salt of choice (*i.e.*, $AuCl_3$, $AgNO_3$, $CuCl_2$, $PdCl_2$, $PtCl_4$). Upon adding the metal salt solution to the GeNS suspension, the Ge–H moieties on the GeNS surfaces immediately react, reduce the metal ions, and deposit size-polydisperse metal particles onto the GeNS surfaces. This process is accompanied by the evolution of bubbles (presumably hydrogen) and a colour change from red to grey/black independent of the metal employed.

Powder X-ray diffraction (XRD) was used to interrogate the nature of the metal deposits on the decorated GeNSs (*i.e.*, M@GeNSs; Fig. 1a and d and S1†). In all cases, M@GeNSs showed broadened reflections characteristic of the target metals superimposed on the (006), (012), (110) and (116) reflections arising from GeNSs.[21] These observations are consistent with the successful deposition of metal nanoparticles and retention of the GeNS structure. The broadening of the characteristic reflections arising from the nanoparticles depends upon the metal in question. Analyses of these reflections provide approximate crystallite sizes (*i.e.*, Au, 17.4 nm; Ag, 27.4 nm; Cu, 35.6 nm; Pd, 12.7 nm; Pt, 4.8 nm) by using the Scherrer equation.[22]

To further investigate the nature of the parent GeNSs and M@GeNSs, we interrogated the materials using Fourier-transform infrared (FTIR) and X-ray photoelectron (XPS) spectroscopies. The FTIR spectrum (Fig. S2†) of the parent GeNSs shows intense features associated with Ge–H stretching (2000 cm^{-1}) and bending modes (830 cm^{-1} and 770 cm^{-1}).[23] Following metal deposition, FTIR spectra of M@GeNSs displayed a prominent feature in the range of 700 to 890 cm^{-1} that we attribute to Ge–O vibrations. We also note that the intensities Ge–H associated features diminished, however they still remain obvious.[24] Our observations are similar to those reported for metal decorated silicane[8] and suggest the surface hydride functionalities have reduced metal ions leaving surface dangling bonds on the GeNSs that are subsequently oxidized to form Ge–O–Ge and Ge–O–H moieties.

Looking to XPS, it provides complementary information related to material composition, as well as bonding environment, and oxidation states of accessible elements in the materials in question. The survey spectrum of the parent GeNSs reveals they comprise Ge, as well as trace Cl (*i.e.*, 1.2 atomic%) and O (*i.e.*, 5.1 atomic%) (Fig. S3†). In contrast, and consistent with our FTIR and XRD analyses (*vide supra*), survey XP spectra of the M@GeNSs show evidence of oxidation and corresponding metal particles (Fig. S5†). Deconvolution of the Ge 3d region of the high-resolution XP spectra gave insight into the speciation of Ge atoms within the parent and metal decorated GeNSs. Parent nanosheets (Fig. S4†) show the expected characteristic Ge emission of germanane at 29.8 eV as well as some Ge^{2+} (31.2 eV; 3.5% of Ge) and Ge^{4+} (32.5 eV; 6.2% of Ge). The metal loadings of M@GeNSs were calculated based upon compositions determined from XP survey spectra integration (Table S1†). The metal loading decreased from Ag, Pd, Cu, Au, and Pt, following the same trend as the charge of the metal ions (*i.e.*, Ag^+, Pd^{2+}, Cu^{2+}, Au^{3+}, and Pt^{4+}).

In all cases, the high-resolution XP spectra of M@GeNSs showed emissions associated with the corresponding metal (*i.e.*, Au, Ag, Cu, Pd, and Pt) deposits and the underlying GeNSs (Fig. S6†). For convenience, the present discussion will be

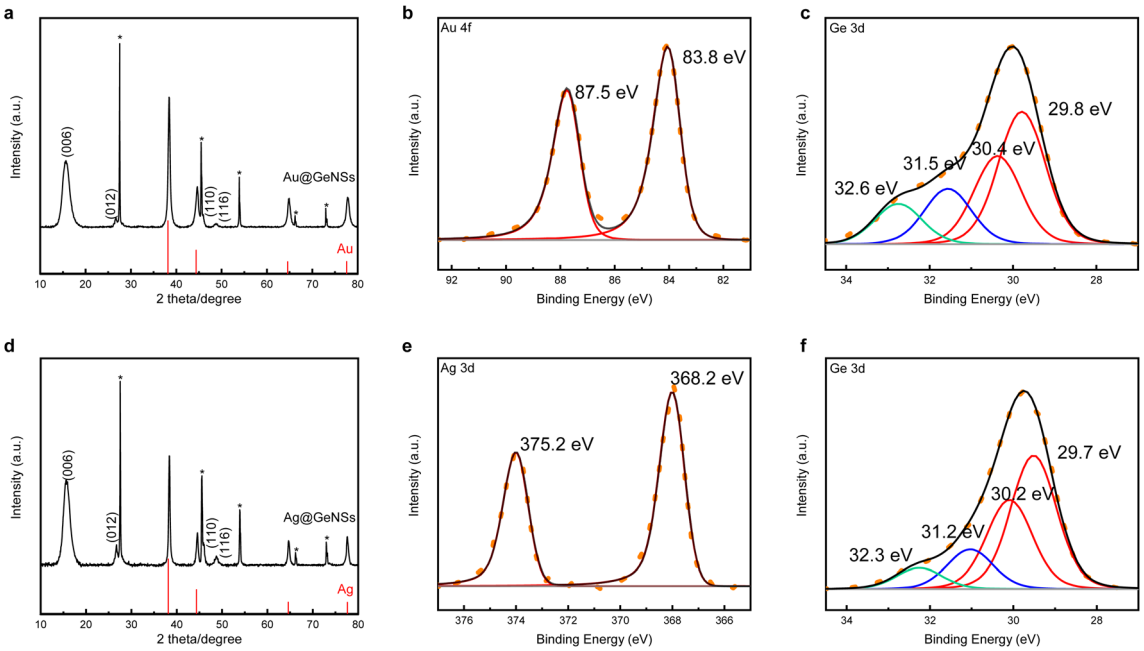

Fig. 1 XRD (a and d) and high resolution XPS analyses (b, c, e and f) of Au@GeNSs (Top) and Ag@GeNSs (Bottom). Reflections marked with asterisks (*) correspond to crystalline Ge.[25] Au and Ag reflections (PDF#89-3697 and 89-3722, respectively) are provided for reference.

limited to the XP spectra of M@GeNSs (M = Au or Ag). Fitting the Ge 3d spectra provides a binding energy of 29.8 eV that has been previously attributed to Ge in the nanosheets.[21] We also note components appearing at 31.3 and 32.5 eV that have previously been attributed to Ge^{2+} and Ge^{4+} species, respectively (Fig. 1c and f).[20] The XP spectra of Au and Ag decorated M@GeNSs (Fig. 1b and e) show emissions at binding energies characteristic of the corresponding metallic state (*i.e.*, Au $4f_{7/2}$, 83.8 eV; Ag $3d_{5/2}$, 368.2 eV). Corresponding data for M@GeNSs (M = Cu, Pd, Pt) are provided in Table S1 and Fig. S6.†

Diffuse reflectance spectroscopy allows direct measurement of the optical band gap of solids. The optical band gaps of M@GeNS are smaller than that of GeNSs (*i.e.*, 1.8 eV) in the range of 1.6 to 1.7 eV and show no obvious dependence on metal speciation. Urbach tails were observed in the analyses of all samples (Fig. S7†) and show some sample to sample variation consistent with varying degrees of disorder and oxidation.[23] Additional absorption edges above 2 eV were also noted that are readily attributed to the metal nanoparticles on the GeNS surfaces.[8]

Electron microscopy of M@GeNSs reveals information regarding material nano-morphology. High-resolution transmission electron microscopy (HRTEM) images confirm the deposition of nanocrystalline Au and Ag particles onto the GeNS surfaces (Fig. 2a and e and S8†). Brightfield TEM reveals the deposited metal nanoparticles are pseudospherical with dimensions in the range of 2.7 to 18.8 nm consistent with the observed XRD reflection peak broadening (Fig. S9†).[26] High-angle annular dark-field scanning transmission electron microscopy (HAADF-STEM) images show M@GeNS morphologies consistent with bright field imaging and confirm MNPs are distributed across the NS surfaces with no evidence of ordering (Fig. 2b and f). Finally, EDX mapping confirms the co-localization of morphological features in brightfield and HAADF-STEM comprise the target metal (Fig. 2c, d, g and h).

Photocatalytic oxidation performance

With a series of M@GeNSs in hand, we chose to explore their possible catalytic activity in light-activated aerobic oxidation of neat benzyl alcohol. This reaction was chosen because the primary source of benzaldehyde is the gas-phase oxidation of toluene[27] or liquid-phase oxidation of benzyl alcohol.[28] Established reactions provide complex byproducts (*i.e.*, benzoic acid and benzyl benzoate) and low conversion efficiencies.[29] Given the established importance of benzaldehyde to cinnamaldehyde, exploring new catalytic pathways to its production is of interest.[11] The photochemical reaction conditions investigated as part of the present study are provided in the Experimental section. Gas chromatography-mass spectrometry (GC-MS) analysis of aliquots extracted from the reaction mixture at regular, predetermined time intervals provided a convenient means for monitoring of the reaction progress.

A comparison of the corresponding reactivity of GeNSs, freestanding metal nanoparticles (MNPs), physical mixtures of freestanding metal nanoparticles and GeNSs (MNPs + GeNSs), and M@GeNSs under identical conditions provides insight into the cooperative roles of the components (Fig. 3 and Table S2†). Upon first inspection, it is immediately clear the oxidation of benzyl alcohol does not proceed in the absence of light or in an inert (*i.e.*, N_2) environment.

We also note that the identity of the catalyst is important. The oxidation of benzyl alcohol to benzaldehyde is not efficiently catalyzed by freestanding metal nanoparticles (*i.e.*, <10%

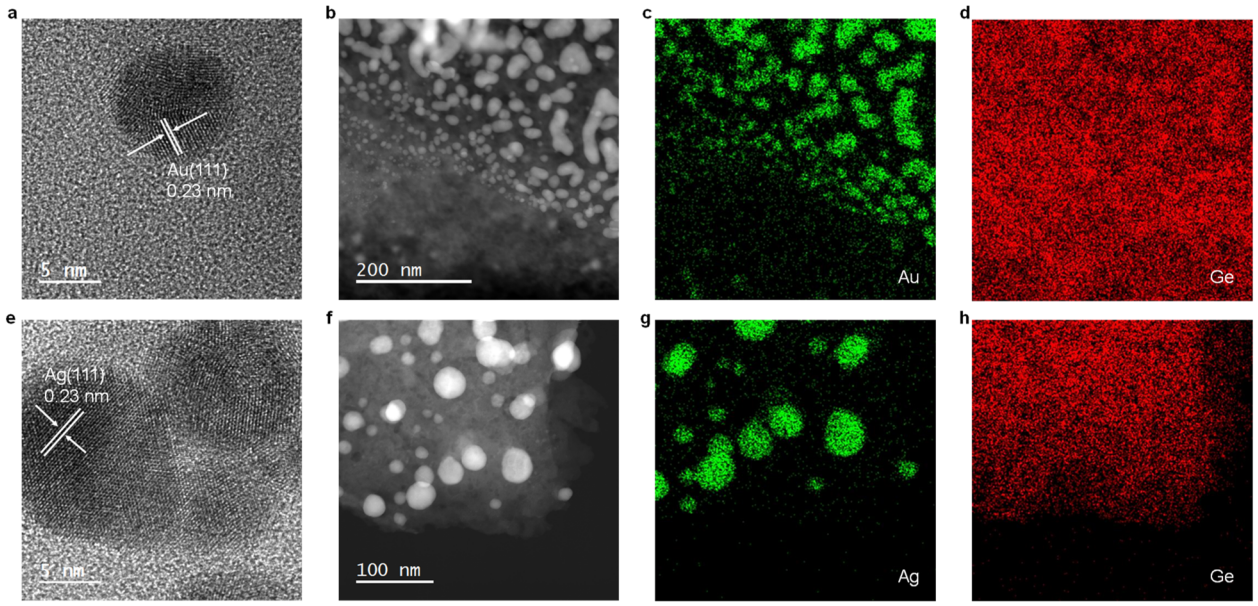

Fig. 2 TEM and EDX analysis of Au@GeNSs (Top) and Ag@GeNSs (Bottom). High-resolution images (a and e) showing characteristic metal (111) lattice spacing. HAADF-STEM images (b and f) and corresponding EDX mapping of the indicated elements (c, d, g and h).

conversion). In this regard, yield and percent selectivity were not evaluated for these systems. Equivalent evaluation of parent, hydrogen-terminated GeNSs show a 30.7% conversion, 82.4% selectivity, and 25.3% yield; GeNSs simultaneously provide the lowest conversion and yield, as well as the highest selectivity of any nanosheet system investigated here. Of import, we also noted the presence of benzoic acid in the product mixture obtained from GeNS suggesting over-oxidation is possible.

To investigate the impact of introducing MNPs on the catalytic activity of M@GeNSs we first explored the reactivity of physical mixtures of MNPs and GeNSs (*i.e.*, MNPs + GeNSs; M = Au, Ag, Cu, Pd, Pt). In all cases, introducing metal nanoparticles prepared *via* solution phase sodium borohydride reduction (*i.e.*, mixtures) provided an apparent increase in percent conversion; however, closer inspection reveals the new higher percent conversion correlates with the straightforward combination of the percent conversions realized by the GeNSs and MNPs alone. This suggests the two nanomaterials are acting independently. Consistent with these observations, FTIR analysis of MNPs (Fig. S11†) suggests they are passivated with O–H and B–O containing functionalities that would prevent direct interaction between the MNPs and GeNSs.[30] A negligible difference between the dimensions of freestanding metal particles and metal particles on GeNSs excludes the influence of metal particle sizes (Table S4†). The question remains: does intimate contact between MNPs and GeNSs influence reactivity.

As noted above, the reducing nature of the hydride surface (*i.e.*, Ge–H) on GeNSs provides a convenient approach toward interfacing GeNSs with MNPs to provide a metal–semiconductor hybrid (*i.e.*, M@GeNSs). FTIR and XPS analyses of these materials (Fig. 1b and e, S2 and S6†) suggest the surfaces of the MNPs in these systems are accessible to solution borne reactants and make these intriguing catalyst candidates. In all cases, other than for reactions involving Au@GeNSs, we note a statistically relevant increase in percent conversion for M@GeNSs catalysts when compared to a straightforward combination of GeNSs, MNPs, and MNP + GeNSs. Ag@GeNSs

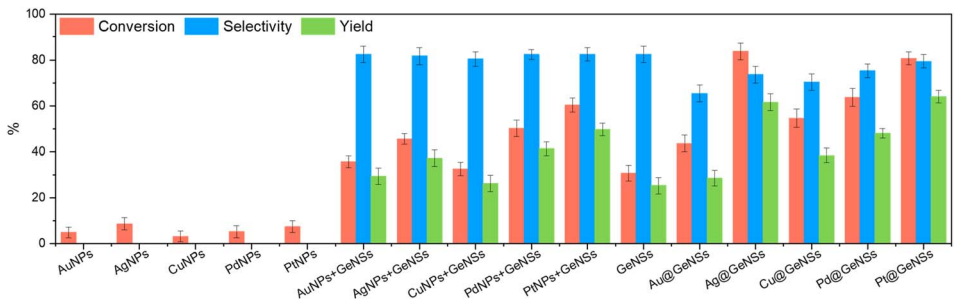

Fig. 3 Photocatalytic oxidation performance: conversion, selectivity and yield of reaction displayed by each of the catalysts for the aerobic oxidation of BA. Associated error bars correspond to mean ± SD ($N = 3$).

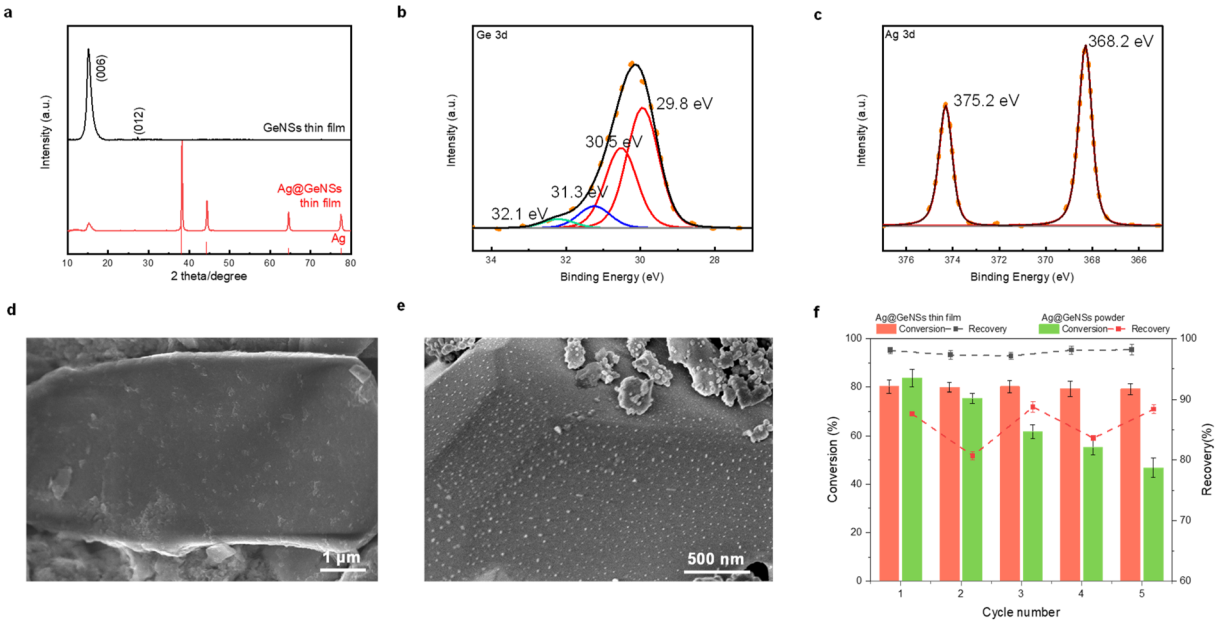

Fig. 4 Characterization and photocatalytic performance of Ag@GeNS thin films: PXRD patterns of (a) Ag@GeNSs and GeNS thin films. High resolution XP spectra of (b) Ge 3d region and (c) Ag 3d region. SEM images of (d) GeNS and (e) Ag@GeNS thin films. Photocatalytic activity and recovery comparison of Ag@GeNS thin film and powder in 5 reaction cycles (f).

exhibit the highest conversion (*i.e.*, 83.7%) with an apparent quantum efficiency (AQE; Fig. S12;† see Experimental section for calculations) of 7.6%. The high-resolution XP spectra of Ag@GeNSs after the reaction showed emissions associated with the corresponding metallic Ag and Ag_2O (Fig. S13a†). The oxidized Ag can further participate in the oxidation of benzyl alcohol without additional oxygen; this would increase conversion while decreasing selectivity (*i.e.*, 73.7%).[31,32] Pt@GeNSs show a slightly lower conversion compared to the Ag analogue (*i.e.*, 80.7%) and higher selectivity for benzaldehyde (*i.e.*, 79.4%) that when combined leads to a higher yield of 64.1%.

The catalytic performance of different loads of Ag on the GeNSs is shown in Table S5.† The conversion of benzyl alcohol increased from 64.6% to 85.4% with increasing Ag loading. However, the selectivity decreased from 76.2% to 71.2% due to the over oxidation of benzaldehyde to benzoic acid by excess Ag.[31] As a result, 5% Ag@GeNSs gave the highest yield of 61.6% (Table S5†). We also note that the presented Ag@GeNSs achieve a considerable conversion rate and selectivity in a short time and moderate condition compared to the already reported literature (Table S6†).

A possible mechanism for the presented catalytic activity of M@GeNSs is shown in Fig. S15.† Initial exposure to UV light homolytically cleaved a Ge–Ge bond providing a "Ge·" radical that can react with surface adsorbed BA. This process leads to the liberation of hydrogen gas and attachment of an R–O moiety to the surface of the GeNS (where R = benzyl) and reformation of the Ge–Ge bond which preserves the integrity of the GeNS. Subsequently, light-induced homolytic cleavage of the benzyl C–H bond provides a carbon-based "C·" radical that can directly react with molecular oxygen that is adsorbed to adjacent MNPs and ultimately lead to the liberation of benzaldehyde.[16,33] Of particular note, this process will also lead to partial oxidation of the underlying GeNS which is evident in the presented XPS and FTIR analyses (Fig. S13b and S14†).

To leverage M@GeNSs as a photocatalyst, the catalyst should ideally exhibit high recovery and reusability. For convenience, we used Ag@GeNSs as an illustration (Fig. 4f) to test the reusability of the present systems. For freestanding Ag@GeNSs the conversion efficiency decreased by nearly half its original value due to the poor recovery after only five cycles; this is not unexpected given the small amount of catalyst employed (*ca.* 40 mg). The nanoscale Ag@GeNSs suspension in the reaction mixture was lost during analyses and recycling. In light of the poor recyclability of the powder catalyst, we prepared Ag@GeNSs thin films to improve their reuse. Ag@GeNS thin films were characterized using XRD, XPS, and SEM (Fig. 4). These analyses revealed that the GeNS crystallinity maintained after the film formation and the intense reflections characteristic of metallic Ag confirm the successful deposition of Ag NPs. High-resolution XP spectra of the Ge 3d region show characteristic emissions from the Ge in the nanosheet at 29.8 eV as well as two less intense emissions from Ge^{2+} and Ge^{4+}. The Ag 3d region showed an emission at 368.2 eV corresponding to metallic Ag. Secondary electron SEM images confirm the expected morphology of GeNSs thin film (Fig. 4d and S16†) and after the deposition of Ag, many dispersed particles with approximate dimensions of *ca.* 20 nm are noted on the GeNS surfaces (Fig. 4e and S16†).

The Ag@GeNSs thin films were evaluated under the same photocatalytic conditions as their freestanding counterparts (see Fig. 4f and Table S7†). From these analyses, we note a marked improvement in recyclability over freestanding systems with thin films showing an average of 97.7% recovery

and 79.8% conversion percent over 5 cycles. Although the catalytic performance during the first cycle is not as high as Ag@GeNSs powder, the excellent recovery provides long-term cycling.

Conclusions

Herein, we have demonstrated a facile method for introducing a variety of adherent metal nanoparticles (Au, Ag, Cu, Pd, Pt) to the surfaces of GeNSs. XRD and XPS analyses confirm that the GeNS structure remained intact during the deposition process and metal nanoparticles were formed. Further, TEM studies revealed the morphology of the M@GeNSs and showed the metal nanoparticles were distributed over the entire GeNS surface. The presented materials were subsequently interrogated as photocatalysts for the selective visible light-induced oxidation of benzyl alcohol. The M@GeNSs possess a higher conversion efficiency compared to a straightforward mixture of freestanding metal nanoparticles prepared *via* solution reduction and GeNSs. The synergistic effect of the intimately linked metal nanoparticles and GeNSs in M@GeNSs strongly favors the production of benzaldehyde *via* oxygen-atom transfer from metal nanoparticles to the product. Furthermore, thin films of metal-decorated GeNSs prepared *via* drop-casting provide for convenient catalyst recovery and recyclability.

Experimental

Materials

Germanium (Ge, 99.999%), calcium (Ca, 99.0%), gold chloride ($AuCl_3$, 99.99%), silver nitrate ($AgNO_3$, 99.9999%), copper chloride ($CuCl_2$, 99.999%), palladium chloride ($PdCl_2$, 99.9%) and platinum chloride ($PtCl_4$, 99.999%) were purchased from Sigma-Aldrich and hydrochloric acid (HCl, 37% w/w), ethanol (anhydrous) dichloromethane (HPLC grade) and toluene (HPLC grade) were purchased from Fisher Scientific. Milli-Q (18.2 MΩ cm at 25 °C) water was used for all experiments. All organic solvents were dried using an Innovative Technology, Inc. Grubbs-type solvent purification system.

Synthesis of $CaGe_2$. A stoichiometric mixture of calcium and germanium metals was pressed into a pellet and subsequently melted together from both sides using an arc furnace.[20]

Synthesis of stacked germanane. Germanane was prepared *via* topotactic deintercalation of calcium ions from $CaGe_2$ using a modified literature procedure.[21] Briefly, 0.3 g (2.7 mmol) of freshly prepared granular $CaGe_2$ was loaded into a Schlenk flask that was charged with concentrated aqueous HCl (30 mL) that had been cooled to −30 °C. The reaction mixture was maintained at −30 °C for at least 7 days and agitated at regular intervals. Subsequently, the reaction mixture was filtered using a glass frit under nitrogen to provide grey flakes that exhibited a metallic sheen that were washed three times with ice-cold Milli-Q water and anhydrous ethanol. The resulting shiny grey solid was dried *in vacuo* on the Schlenk line and stored in a nitrogen-filled glovebox and subdued light until further use.

Preparation of metal-decorated germanium nanosheets (M@GeNSs). To prepare metal-decorated germanium nanosheets (M@GeNSs; M = Au, Ag, Cu, Pt, Pd), germanane powder (73 mg; 1 mmol) was dispersed in 4 mL distilled water. The mixture was sonicated in a bath sonicator for 2 hours to yield a red suspension of exfoliated GeNSs. Subsequently, an appropriate mass (0.05 mmol) of the anhydrous metal salt in question ($AuCl_3$, $AgNO_3$, $CuCl_2$, $PdCl_2$ and $PtCl_4$) was dissolved in 1 mL of Milli-Q water. The metal salt solution (*i.e.*, 0.1 mL) was then added into the GeNS dispersion at room temperature in subdued light and the original red suspensions turned black. The mixture was stirred for 10 min and the product was recovered by centrifugation and washed with Milli-Q water three times. The product was dried for 12 h *in vacuo* and subsequently stored in a nitrogen-filled glovebox and subdued light. Typical mass yields for this procedure were 55 mg. The resulting material was characterized using XRD, XPS, and TEM.

Fabrication of thin films of GeNSs and Ag@GeNSs. Thin films of GeNSs were deposited onto glass substrates by first suspending GeNSs (73 mg, 1 mmol) in 1,3-dioxane (1 mL) with sonication for 30 min. Subsequently, a 100 μL aliquot of the suspension was drop-coated onto a glass substrate that had been precleaned by ethanol, acetone and Milli-Q water and dried in a vacuum oven for 2 h. The glass-supported GeNS thin films were subsequently immersed in 10 mL of aqueous $AgNO_3$ (0.05 mmol) for 10 min. Upon removing the film from the $AgNO_3$ solution, the films were rinsed with 5 mL Milli-Q water three times and dried in a stream of flowing dry N_2 gas. The films were transferred to a nitrogen-filled glovebox and maintained in subdued light.

Preparation of unsupported metal nanoparticles. Unsupported metal nanoparticles (MNPs) used for comparison with GeNS-supported catalysts were synthesized *via* $NaBH_4$ reduction.[34] Typically, 0.05 mol metal salt (*i.e.*, $AuCl_3$, $AgNO_3$, $CuCl_2$, $PdCl_2$, $PtCl_4$) was dissolved in 25 mL Milli-Q water and vigorously stirred at room temperature in air. Subsequently, aqueous sodium borohydride ($NaBH_4$, 100 mM, 1 mL) was rapidly injected into the metal salt solution, immediately leading to a light-yellow solution. This process was also accompanied by the evolution of bubbles. After 5 min, the colloidal solution turned to a deep yellow due to the formation of small nanoparticles. Then the MNPs were isolated by centrifugation, resuspended with sonication in 5 mL ethanol. This suspension/centrifugation procedure was repeated three times with 5 mL of Milli-Q water. Finally, the resulting MNPs were stored in Milli-Q water until further use.

Characterization

Fourier transformed infrared (FTIR) spectroscopy. Analyses were performed using a Thermo Nicolet 8700 FTIR Spectrometer and Continuum FTIR Microscope. Samples were prepared by drop coating a toluene dispersion of the solid sample in question onto an electronics-grade Si-wafer (N-type, 100 surface, 100 mm thickness and 10 ohm cm resistivity) and dried under flowing nitrogen.

Electron microscopy. Transmission electron microscopy (TEM) bright and dark field images were acquired using a JEOL JEM-ARM200CF S/TEM electron microscope at an accelerating

voltage of 200 kV. High resolution (HR) TEM images were processed using Gatan Digital Micrograph software (Version 3.4.1). TEM samples were prepared by depositing a drop of a dilute toluene suspension of the sample in question onto a holey or ultra-thin carbon-coated copper grid (obtained from Electron Microscopy Inc.). The grid bearing the sample was kept in a vacuum chamber at a base pressure of 0.2 bar for at least 24 h prior to data collection. The particle size distribution was assembled as an average shifted histogram as described by Buriak *et al.* for at least 300 particles in TEM.[35]

Secondary electron scanning electron microscopy (SEM) images were acquired using a Hitachi S4800 FESEM electron microscope at an accelerating voltage of 10 kV. Samples were mounted on a stainless-steel stub by using conductive tape.

X-ray photoelectron spectroscopy (XPS). XPS analyses were performed using a Kratos Axis Ultra instrument operating in energy spectrum mode at 210 W. The base and operating chamber pressure were maintained at 10^{-7} Pa. A monochromatic Al Kα source ($\lambda = 8.34$ Å) was used to irradiate the samples, and the spectra were obtained with an electron take-off angle of 90°. CasaXPS software (VAMAS) was used to interpret high-resolution spectra. All spectra were internally calibrated to the C 1s emission (284.8 eV) of adventitious carbon. After calibration, a Shirley-type background was applied to remove most of the extrinsic loss structure. The Ge 3d region was deconvoluted into the Ge $3d_{5/2}$ and $3d_{3/2}$ spin–orbit couple for the element Ge and the energy separation of these doublets was fixed at 0.58 eV and the Ge $3d_{3/2}$ to $3d_{5/2}$ area was fixed at 0.67.[20] For the high-resolution XP spectra of metals, the spin–orbit couple energy separation and area were fixed and the spectral envelope was fit using a Lorentzian asymmetric line shape LA(a, b, n) where a and b define the asymmetry and n defines the Gaussian width. The various spectral regions were fit as follows: Au 4f was deconvoluted into the Au $4f_{7/2}$ and $4f_{5/2}$ spin–orbit couple and the energy separation of these doublets was fixed at 3.70 eV and the Au $4f_{7/2}$ to $4f_{5/2}$ area ratio was fixed at 0.75.[36] Ag 3d was deconvoluted into the Ag $3d_{5/2}$ and $3d_{3/2}$ spin–orbit couple and the energy separation of these doublets was fixed at 6.00 eV and the Ag $3d_{3/2}$ to $3d_{5/2}$ area ratio was fixed at 0.67.[31] Cu 2p was deconvoluted into the Cu $2p_{3/2}$ and $2p_{1/2}$ spin–orbit couple and the energy separation of these doublets was fixed at 19.75 eV and the Cu $2p_{3/2}$ and $2p_{1/2}$ area ratio was fixed at 0.50.[37] Pd 3d was deconvoluted into the Pd $3d_{5/2}$ and $3d_{3/2}$ spin–orbit couple and the energy separation of these doublets was fixed at 5.26 eV and the Ag $3d_{3/2}$ to $3d_{5/2}$ area ratio was fixed at 0.67.[38] Pt 4f was deconvoluted into the Pt $4f_{7/2}$ and $4f_{5/2}$ spin–orbit couple and the energy separation of these doublets was fixed at 3.35 eV and the Pt $4f_{7/2}$ to $4f_{5/2}$ area ratio was fixed at 0.75.[39]

Powder X-ray diffraction (XRD) analysis. XRD was performed using a Bruker D8 Advance diffractometer (Cu-$K_{\alpha 1}$ ($\lambda = 1.5406$ Å) and $K_{\alpha 2}$ ($\lambda = 1.5444$ Å) radiation). Samples were prepared by mounting the powder in question on a zero background Si crystal sample holder. XRD patterns were scanned between 2θ ranges of 10–80° with a scan step of 0.06° s^{-1}.

Diffuse reflective absorption. Diffuse reflective absorption analysis was performed using a CARY 5000 UV-vis-NIR equipped with a diffuse reflectance integrating sphere attachment. Samples were prepared by mounting the powder sample of interest in the sample holder. The detector and grading filter were changed at 900 nm.

Photocatalytic oxidation of benzyl alcohol

Photocatalytic oxidation of benzyl alcohol was performed using a modified literature procedure.[16] A typical reaction was performed using a Schlenk flask charged with benzyl alcohol (40 mL; 380 mmol), catalyst of choice (total mass: 22 mg; 0.02 mmol of metal), and a new Teflon-coated stir bar. The reaction vessel was evacuated and backfilled 5 times with oxygen and finally maintained under a positive pressure of bubbling oxygen during the reaction. The reaction mixture was then stirred at 1500 rpm for 0.5 h after which it was exposed to the emission of a 140 W Hg lamp (Hanovia, wavelength > 366 nm, photon flux 8×10^{17} s^{-1}). The reaction vessel was thermostated by immersing it in a water bath maintained at 25 °C. The reaction was carried out for 4 h and aliquots (4 mL) were extracted from the reaction mixture every 30 min and diluted to a total volume of 400 mL using dichloromethane and the diluted solution was evaluated using gas chromatography-mass spectrometry (Bruker SCION TQ with 456-GC). The molar concentration of each component was determined using calibration curves prepared using standards of known concentrations. The conversion percentage (C) of benzyl alcohol (BA) and the selectivity (S) and the yield (Y) for benzaldehyde (BAL) are defined as:

$$C(\%) = \frac{n(\mathrm{BA}_0) - n(\mathrm{BA})}{n(\mathrm{BA}_0)} \times 100\% \quad (1)$$

$$S(\%) = \frac{n(\mathrm{BAL})}{n(\mathrm{BA}_0) - n(\mathrm{BA})} \times 100\% \quad (2)$$

$$Y(\%) = \frac{n(\mathrm{BAL})}{n(\mathrm{BA}_0)} \times 100\% \quad (3)$$

where $n(\mathrm{BA}_0)$ is the initial mole of BA and n(BA) and n(BAL) are the moles of the detected BA and BAL, respectively.

Generally, the apparent quantum efficiency (AQE) of the reaction is the ratio between the photons taking part in the reaction and the total number of incident photons:

$$\mathrm{AQE}(\%) = \frac{N(\mathrm{BAL})}{I} \times 100\% \quad (4)$$

where N(BAL) represents the number of molecules of BAL produced, and I is the number of incident photons.[9]

Catalyst recycling

The recyclability/reusability of the powder catalysts and thin films was evaluated by performing reactions under identical conditions as described above. A total of 5 cycles were performed for each sample. After each cycle, the powder catalyst was recovered by centrifugation, washed with 5 mL Mill-Q water three times and dried under vacuum and finally massed; thin films were rinsed with 5 mL Mill-Q water three times and dried

with flowing N_2 gas and massed. The recovery percentage was determined based upon the difference between the weight before and after each cycle.

Author contributions

Chuyi Ni: conceptualization, methodology, investigation, formal analysis, investigation, data curation, and writing – original draft. Madison Chevalier: investigation, data curation, and writing – review & editing. Jonathan G. C. Veinot: supervision, conceptualization, methodology, formal analysis, investigation, data curation, resources, funding acquisition, and writing – review & editing. All authors discussed the results and the implications of this manuscript. All authors have given approval to the final version of the manuscript.

Conflicts of interest

There are no conflicts to declare.

Acknowledgements

The authors recognize the continued generous funding from the Natural Science and Engineering Research Council (NSERC Discovery Grant program; RGPIN-2020-04045), the ATUMS training program supported by NSERC CREATE (CREATE-463990-2015) as well as the University of Alberta Faculties of Science and Graduate Studies, and Alberta Innovates Strategic Projects Program. We also thank the staff at Analytical and Instrumentation Laboratory in the Department of Chemistry at the University of Alberta for the assistance with FTIR analysis, and the University of Alberta Nanofab for support in collecting XPS data.

References

1 W. L. B. Huey and J. E. Goldberger, *Chem. Soc. Rev.*, 2018, **47**, 6201–6223.
2 S. Jiang, K. Krymowski, T. Asel, M. Q. Arguilla, N. D. Cultrara, E. Yanchenko, X. Yang, L. J. Brillson, W. Windl and J. E. Goldberger, *Chem. Mater.*, 2016, **28**, 8071–8077.
3 T. Helbich, A. Lyuleeva, P. Marx, L. M. Scherf, T. K. Purkait, T. F. Fässler, P. Lugli, J. G. C. Veinot and B. Rieger, *Adv. Funct. Mater.*, 2017, **27**, 1606764.
4 T. Hartman and Z. Sofer, *ACS Nano*, 2019, **13**, 8566–8576.
5 Z. Liu, Z. Lou, Z. Li, G. Wang, Z. Wang, Y. Liu, B. Huang, S. Xia, X. Qin, X. Zhang and Y. Dai, *Chem. Commun.*, 2014, **50**, 11046–11048.
6 Z. Liu, Z. Wang, Q. Sun, Y. Dai and B. Huang, *Appl. Surf. Sci.*, 2019, **467–468**, 881–888.
7 S. Ng, J. Sturala, J. Vyskocil, P. Lazar, J. Martincova, J. Plutnar and M. Pumera, *ACS Nano*, 2021, **15**, 11681–11693.
8 C. Qian, W. Sun, D. L. H. Hung, C. Qiu, M. Makaremi, S. G. Hari Kumar, L. Wan, M. Ghoussoub, T. E. Wood, M. Xia, A. A. Tountas, Y. F. Li, L. Wang, Y. Dong, I. Gourevich, C. V. Singh and G. A. Ozin, *Nat. Catal.*, 2018, **2**, 46–54.
9 F. Zhao, Y. Feng, Y. Wang, X. Zhang, X. Liang, Z. Li, F. Zhang, T. Wang, J. Gong and W. Feng, *Nat. Commun.*, 2020, **11**, 1443.
10 M. Aizawa, A. M. Cooper, M. Malac and J. M. Buriak, *Nano Lett.*, 2005, **5**, 815–819.
11 H. H. Richmond, *US Pat.*, 73966147A, 1950.
12 D. I. Enache, J. K. Edwards, P. Landon, B. Solsona-Espriu, A. F. Carley, A. A. Herzing, M. Watanabe, C. J. Kiely, D. W. Knight and G. J. Hutchings, *Science*, 2006, **311**, 362–365.
13 J. Long, X. Xie, J. Xu, Q. Gu, L. Chen and X. Wang, *ACS Catal.*, 2012, **2**, 622–631.
14 S. Furukawa, T. Shishido, K. Teramura and T. Tanaka, *ACS Catal.*, 2011, **2**, 175–179.
15 M. A. Patel, F. Luo, M. R. Khoshi, E. Rabie, Q. Zhang, C. R. Flach, R. Mendelsohn, E. Garfunkel, M. Szostak and H. He, *ACS Nano*, 2016, **10**, 2305–2315.
16 W. Feng, G. Wu, L. Li and N. Guan, *Green Chem.*, 2011, **13**, 3265–3272.
17 X. Huang, O. Akdim, M. Douthwaite, K. Wang, L. Zhao, R. J. Lewis, S. Pattisson, I. T. Daniel, P. J. Miedziak, G. Shaw, D. J. Morgan, S. M. Althahban, T. E. Davies, Q. He, F. Wang, J. Fu, D. Bethell, S. McIntosh, C. J. Kiely and G. J. Hutchings, *Nature*, 2022, **603**, 271–275.
18 M. Qamar, R. B. Elsayed, K. R. Alhooshani, M. I. Ahmed and D. W. Bahnemann, *ACS Appl. Mater. Interfaces*, 2015, **7**, 1257–1269.
19 L. Jia, D.-H. Wang, Y.-X. Huang, A.-W. Xu and H.-Q. Yu, *J. Phys. Chem. C*, 2011, **115**, 11466–11473.
20 H. Yu, A. N. Thiessen, M. A. Hossain, M. J. Kloberg, B. Rieger and J. G. C. Veinot, *Chem. Mater.*, 2020, **32**, 4536–4543.
21 H. Yu, T. Helbich, L. M. Scherf, J. Chen, K. Cui, T. F. Fässler, B. Rieger and J. G. C. Veinot, *Chem. Mater.*, 2018, **30**, 2274–2280.
22 U. Holzwarth and N. Gibson, *Nat. Nanotechnol.*, 2011, **6**, 534.
23 E. Bianco, S. Butler, S. Jiang, O. D. Restrepo, W. Windl and J. E. Goldberger, *ACS Nano*, 2013, **7**, 4414–4421.
24 L. Khomenkova, D. Lehninger, O. Kondratenko, S. Ponomaryov, O. Gudymenko, Z. Tsybrii, V. Yukhymchuk, V. Kladko, J. von Borany and J. Heitmann, *Nanoscale Res. Lett.*, 2017, **12**, 196.
25 N. D. Cultrara, Y. Wang, M. Q. Arguilla, M. R. Scudder, S. Jiang, W. Windl, S. Bobev and J. E. Goldberger, *Chem. Mater.*, 2018, **30**, 1335–1343.
26 C. F. Holder and R. E. Schaak, *ACS Nano*, 2019, **13**, 7359–7365.
27 A. Brückner, *Appl. Catal., A*, 2000, **200**, 287–297.
28 G. Zhan, Y. Hong, V. T. Mbah, J. Huang, A.-R. Ibrahim, M. Du and Q. Li, *Appl. Catal., A*, 2012, **439–440**, 179–186.
29 C. P. Ferraz, M. A. S. Garcia, É. Teixeira-Neto and L. M. Rossi, *RSC Adv.*, 2016, **6**, 25279–25285.
30 C. Gautam, A. K. Yadav and A. K. Singh, *ISRN Ceram.*, 2012, **2012**, 1–17.
31 L. Ma, l. Jia, X. Guo and L. Xiang, *Chin. J. Catal.*, 2014, **35**, 108–119.
32 L. Jia, S. Zhang, F. Gu, Y. Ping, X. Guo, Z. Zhong and F. Su, *Microporous Mesoporous Mater.*, 2012, **149**, 158–165.

33 F. Xie, Y. Zhang, X. He, H. Li, X. Qiu, W. Zhou, S. Huo and Z. Tang, *J. Mater. Chem. A*, 2018, **6**, 13236–13243.
34 Q. Zhang, N. Li, J. Goebl, Z. Lu and Y. Yin, *J. Am. Chem. Soc.*, 2011, **133**, 18931–18939.
35 S. L. Anderson, E. J. Luber, B. C. Olsen and J. M. Buriak, *Chem. Mater.*, 2016, **28**, 5973–5975.
36 Y. Zhang, X. Han, R. Liu, Y. Liu, H. Huang, J. Zhang, H. Yu and Z. Kang, *J. Phys. Chem. C*, 2012, **116**, 20363–20367.
37 M. C. Biesinger, *Surf. Interface Anal.*, 2017, **49**, 1325–1334.
38 M. C. Militello and S. J. Simko, *Surf. Sci. Spectra*, 1994, **3**, 387–394.
39 C. R. O'Connor, M. A. Van Spronsen, M. Karatok, J. Boscoboinik, C. M. Friend and M. M. Montemore, *J. Phys. Chem. C*, 2021, **125**, 10685–10692.